Materials Advances

ROYAL SOCIETY OF CHEMISTRY

PAPER

View Article Online
View Journal | View Issue

Cite this: *Mater. Adv.*, 2024, 5, 8053

Thermoelectric properties of $YbZn_{11-x}Al_x$†

Shuai Li,[a] Ruhul Quddus,[b] Sree Sourav Das,[b] Haobo Wang,[a] Jerrold A. Floro[a] and Mona Zebarjadi *[ab]

Received 17th June 2024,
Accepted 8th September 2024

DOI: 10.1039/d4ma00626g

rsc.li/materials-advances

Metallic thermoelectric materials with a high thermoelectric power factor and high thermal conductivity are favorable for transient dynamic active thermal management of microelectronics. Among these, several ytterbium intermetallic compounds demonstrate sharp peaks in their density of states due to contributions from ytterbium f-orbitals. $YbZn_{11}$ is one of these compounds with a Gaussian-like density of states close to its Fermi level, an advantageous shape to achieve a high thermoelectric power factor. If the Fermi-level can be adjusted, high Seebeck coefficient values are expected following the Wiedemann–Franz law. Here we present $YbZn_{11}$, a rarely made and studied sample, and for the first time, we report its thermoelectric and transport properties. Band structure calculations confirm the Gaussian function shape of the density of states. However, Seebeck calculations show that the Fermi level is not well positioned and ideally should be shifted by 200 meV. Al substitution for Zn ($YbZn_{11-x}Al_x$) and Zn-deficiency ($YbZn_{11-x}$) are applied to modify the band structure and to shift the Fermi level to adjust the Seebeck coefficient.

1. Introduction

State-of-the-art electronics featuring high-power chips pack gigahertz transistors in an extremely dense manner. The substantial heat accumulated in such a small area presents new challenges for thermal management.[1–3] The concept of the thermoelectric (TE) active cooling mode provides innovative approaches for active heat management.[4,5] Unlike traditional thermoelectric modes with the Seebeck voltage (Peltier current) working against the temperature gradient, in the active cooling mode, the natural heat conduction from the hot source to the heat sink is enhanced by the Peltier current. The Peltier current, driven by the electric current, propels carriers along the temperature gradient, augmenting the passive transport of electrons and phonons. The TE module functions as an active heat sink. The effective thermal conductivity of this active heat sink under optimal current conditions is expressed as $\kappa_{\text{eff}} = \left(\kappa + \frac{\sigma S^2 T_H^2}{2\Delta T}\right)$, where T_H is the hot source temperature, ΔT is the temperature difference between the hot source and the heat sink, κ is the passive thermal conductivity, σ is the electrical conductivity, and S is the Seebeck coefficient.[5] Hence to maximize the effective thermal conductivity, materials with high TE power factors (σS^2) and high passive thermal conductivity values (κ) are needed.

Metals are great candidates for this application due to their inherently high electrical and thermal conductivity. Their only drawback is their low Seebeck coefficient. Hence, one can search for metals with high Seebeck coefficients to satisfy all criteria needed for successful active cooling. Pure metallic elements such as cobalt and nickel are shown to have a relatively high Seebeck coefficient. Various mechanisms can improve the Seebeck coefficient in metals. For instance, in the case of cobalt, the higher Seebeck coefficient is attributed to the magnon-drag effect.[4] In $CePd_3$ the electron correlation effect results in a Seebeck coefficient of more than 115 $\mu V\ K^{-1}$ at 150 K.[4] The Kondo resonance caused by the interaction of Yb 4f-orbital electrons and conduction bands gives $YbAl_3$ a Seebeck coefficient of $-90\ \mu V\ K^{-1}$ below room temperature.[6] The Cu–Ni alloy, also known as constantan, shows an improved Seebeck coefficient of $-45.7\ \mu V\ K^{-1}$ at room temperature and $-72.5\ \mu V\ K^{-1}$ at 873 K due to the scattering of low-energy carriers by nano-twin boundaries.[7] A further study explored the possibility of additive manufacturing of the Cu–Ni alloy using industrial-level powders.[8] An even higher Seebeck of 94 $\mu V\ K^{-1}$ is achieved in the Ni–Au alloy at 1000 K, which is attributed to the interband scattering between s and d-orbital electrons.[9]

In metals, the Mott formula[10] relates the Seebeck coefficient to the slope of the density of states (DOS) at the Fermi level. For metals, therefore, a sharp peak of the DOS near the Fermi level indicates the potential of a high Seebeck coefficient.[11–14] Some of the Yb-based intermetallic compounds show such features according to first-principles calculations. A good example is

[a] *Department of Materials Science and Engineering, University of Virginia, Charlottesville, VA, 22904, USA. E-mail: m.zebarjadi@virginia.edu*
[b] *Electrical and Computer Engineering Department, University of Virginia, Charlottesville, VA, 22904, USA*

† Electronic supplementary information (ESI) available. See DOI: https://doi.org/10.1039/d4ma00626g

$YbAl_3$ which has a sharply peaked DOS due to the f-orbitals and as a result has a record high thermoelectric power factor.[15] $YbZn_{11}$ is another candidate in this class of materials. Since its crystal structure was first reported in 1966,[16] $YbZn_{11}$ has received little attention. Apart from a few studies that mention it while exploring the phase space of related systems,[17,18] the only paper discussing its inter-band interaction dates to 1998.[19] Moreover, the thermoelectric properties of $YbZn_{11}$ have never been thoroughly examined or reported.

The expected sharp peaks in the DOS of several intermetallic Yb-based compounds are confirmed by band structure calculations from the Topological Materials Database[20–23].[13,15] Similarly, in $YbZn_{11}$, a sharp peak of DOS near the Fermi level is shown in the topological materials database which in principle should result in a high Seebeck coefficient as evidenced by the Mott equation. However, this material is rarely studied, and its thermoelectric properties have never been reported. To assess the guidance provided by computational results and investigate the unreported thermoelectric properties of the materials, we synthesized $YbZn_{11}$. Here, we report structural characterization and assessment of defects, followed by intrinsic thermoelectric properties. Finally, we explore avenues to enhance the thermoelectric performance using doping.

2. Methods

2.1 Experimental methods

Sublimed Yb pieces with 99.9% purity and 99.999% zinc shot were mixed to the stoichiometry of $YbZn_{11}$. The mixed pure metals were loaded into a fused quartz glass tube. The tube was evacuated and backfilled with argon three times, and then sealed. The sealed ampoule was heated up to 890 °C to melt the metal for 16 hours, and then kept at 760 °C for 16 hours. After cooling down the ingot is ground into powder with a mortar and pestle. Ball-milling was not attempted due to the reactive nature of ytterbium. X-ray diffraction (XRD) was performed on powders and hot-pressed samples to confirm the formation of the compound. Al was used to substitute Zn to adjust the Fermi level. 99.999% aluminium powder and wires were added according to stoichiometry. The intrinsic and $YbZn_{10.7}Al_{0.3}$ samples were annealed at 650 °C in a sealed tube for 24 hours, to improve the Al distribution and substitution. For each sample around 2.5 grams of the product powder was loaded in a graphite die, with graphite paper covering the inner wall and the interface between the powder and the pushing rod to prevent sticking. The powders were then hot-pressed at 650 °C under 56 MPa pressure for 300 seconds using an OTF-1700X-RHP4 hot-press setup from MTI Corporation. The hot press chamber was filled with argon gas during the process. A disc-shaped solid sample with a diameter of 12.7 mm was obtained after polishing the hot-pressed ingot. The disc-shaped sample was then cut using a Mager BR220 precision cut-off saw into bar-shaped samples with approximately 2 mm × 2 mm × 10 mm dimensions. Transport performance is determined using the quantum design PPMS Versalab. XRD characterization is performed using an Empyrean X-ray diffractometer from Malvern-Panalytical on a pressed disc sample. Imaging is performed on an FEI Quanta 650 scanning electron microscope (SEM).

2.2 Computational methods

$YbZn_{11}$ crystallizes in a tetragonal $I4_1/amd$ space group with 2 Yb and 22 Zn atoms in the unit cell. The lattice parameters were nominally $a = b = 10.66$ Å and $c = 6.383$ Å from the topological materials database.[1] First-principles calculations were performed using density functional theory (DFT) as implemented in the QUANTUM ESPRESSO package.[24] We used Perdew–Burke–Ernzerhof generalized gradient approximation (PBEsol)[25] pseudopotential for zinc (Zn) and Wentzcovitch (PAW) pseudopotential[26] for ytterbium (Yb). Scalar relativistic pseudopotentials were used throughout the calculation as we found no spin–orbit coupling (SOC) effects on the electronic band structure as shown in the ESI,† Fig. S2. The electronic structure calculation employed a kinetic energy cutoff of 60 Ry with a charge density cutoff of 320 Ry and a Monkhorst–Pack k-point mesh of 8 × 6 × 6. The atomic positions were relaxed through the Broyden–Fletcher–Goldfarb–Shanno (BFGS) algorithm. The convergence threshold of energy was set to 4.8×10^{-9} Ry in the self-consistent calculation. A Gaussian smearing value of 0.01 Ry was chosen during the calculations. Finally, the Seebeck coefficient was evaluated using the BoltzTraP package.[27] BoltzTraP solves the Boltzmann transport equations (BTE) under constant relaxation time approximation.[27] Within the constant relaxation-time approximation, the Seebeck coefficient can be obtained directly from the electronic structure without any adjustable parameters, and it is expressed in the following equation:

$$S_{\alpha\beta}(T,\mu) = \frac{1}{eT\Omega\sigma_{\alpha\beta}(T,\mu)}\int\sigma_{\alpha\beta}(\varepsilon)(\varepsilon-\mu)\left[-\frac{\delta f_0(T,\varepsilon,\mu)}{\delta\varepsilon}\right]d\varepsilon \quad (1)$$

where Ω is the cell volume, e is the electron charge, μ is the chemical potential, ε is the electron energy, and T is the absolute temperature. f_0 is the equilibrium Fermi–Dirac distribution function and $\sigma_{\alpha\beta}$ is the transport distribution tensor with α and β as the tensor indices indicating the crystallographic directions. $\sigma_{\alpha\beta}(\varepsilon)$ is also referred to as the differential conductivity and is $\sigma_{\alpha\beta}(\varepsilon) = v_g{}^2\tau(\varepsilon)g(\varepsilon)$, where v_g is the group velocity, τ is the scattering time, and $g(\varepsilon)$ is the DOS. Under constant relaxation time approximation used here, $\tau(\varepsilon) = \tau_0$ and is a constant and the elements of the conductivity tensor are calculated using the Fourier interpolation of the band structure only.

3. Results and discussion

3.1 Material characterization

Many samples were prepared including intrinsic $YbZn_{11}$, Al-doped ones ($YbZn_{11-x}Al_x$), and Zn-deficient ones ($YbZn_{11-x}$).

The XRD results of three representative samples are shown in Fig. 1. Note that in the patterns of $YbZn_{11}$ and $YbZn_{10.7}Al_{0.3}$, two minor peaks of graphite and Yb_2O_3 can be identified. The graphite peak comes from the residue of graphite paper during the hot pressing process and only exists at the surface. The residue can stay in small cavities during the polishing process.

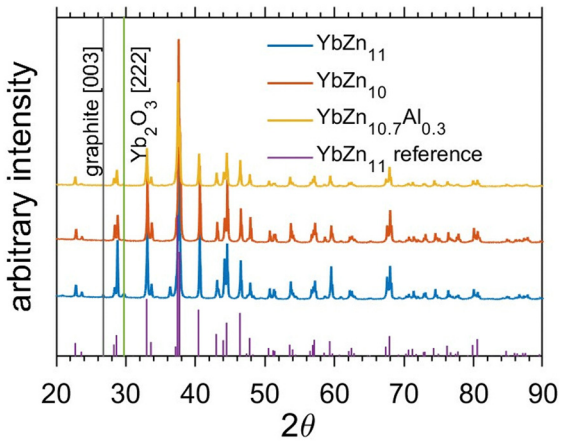

Fig. 1 XRD results of Yb–Zn samples, the annealed intrinsic $YbZn_{11}$ sample in blue, the Zn-deficient sample $YbZn_{10}$ sample in orange, and the Al-substitution sample $YbZn_{10.7}Al_{0.3}$ in yellow, and the reference peaks in purple.[28] Minor impurity peaks from graphite and ytterbium oxide are marked by black and green lines.

The oxide peaks may result from residual oxygen in the sealing process. All the relevant samples show excellent correspondence between the XRD pattern of the synthesized material and the standard diffraction pattern of $YbZn_{11}$ and the impurities only appear in a small volume fraction as indicated by the few identifiable minor peaks in XRD.

SEM micrographs of the $YbZn_{11}$ sample in Fig. 2 show the typical defects in these Yb–Zn intrinsic samples. Fig. 2(a) and (b) show the secondary electron (SE) image and back-scattered electron (BSE) image of the $YbZn_{11}$ sample with a scale bar of 200 μm. $YbZn_{11}$, shown as the extended light grey area in the BSE image, constitutes the majority of material corresponding well with the XRD results. With higher magnification (Fig. 2(c) and (d), SE, and BSE respectively), the impurities in the microstructure can be identified. Typical defects are pores (black), Yb-rich (white), and Zn-rich (dark grey).

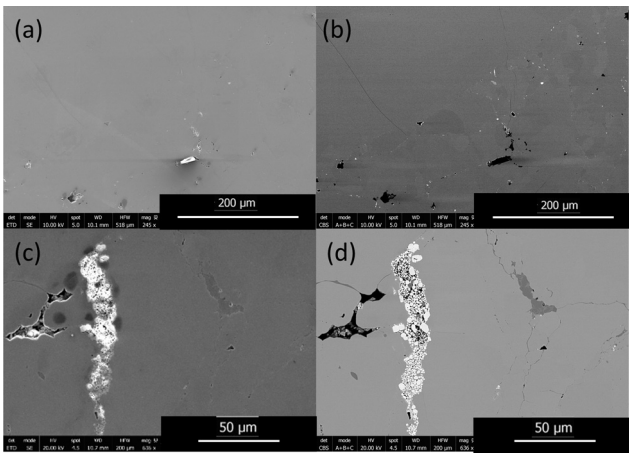

Fig. 2 (a) and (b) The secondary electron (SE) image and back-scattered electron (BSE) image of the $YbZn_{11}$ sample at a larger scale (with a scale bar of 200 μm) at the same site. The bright feature shown in SE image (a) is charging from a glass fragment coming from the synthesis process, which can be confirmed by the fact that the BSE image shows a low electron count from back-scattering, indicating low mass elements. (c) and (d) SE and BSE images at higher magnification (scale bar of 50 μm) on typical defects.

The samples are sintered from hand-milled powders. The intrinsic limitation of this sintering process results in minor retained porosity, as shown in the BSE images. This observation is confirmed by the SE image, which illustrates the morphology. The mass density of the $YbZn_{11}$ sample is measured to be 98% of the theoretical density indicating the presence of some pores. Small Yb pieces that remained un-melted during the melting process or precipitated after cooling oxidized post-process, exhibiting higher brightness in the SE image due to the charging effect and in the BSE image owing to their higher relative mass.

In the EDS mapping mode, the distribution of the elements can be demonstrated clearly as shown in Fig. 3. All three types of defects: cavity (pores), Yb-rich, and Zn-rich phases are shown in one site. In Fig. 3(b), Yb-rich, Zn-rich, and pure $YbZn_{11}$ phases are identified by the red, dark blue, and blue areas, respectively. Fig. 3(c) and (d) show that the defects are caused by unreacted Yb and Zn. The dark grey area in Fig. 3(a) shows a higher Zn concentration as confirmed in Fig. 3(c) and near-zero Yb concentration as confirmed in Fig. 3(d), indicating the existence of the Zn-rich phase. Similarly, the white area in Fig. 3(a) seems to predominantly contain Yb with almost no Zn. Here we postulate that these small defects are ytterbium oxide considering the reactivity of Yb, Yb_2O_3 peaks in XRD, and the charging effect of this kind of defect under the electron beam. Further EDS line scan on the same site crossing all separate phases as shown in Fig. 4 confirms the weight percentage of Yb and Zn in these phases. The main matrix shows the correct weight percentage of Yb and Zn for $YbZn_{11}$, combined with XRD results and EBSD results in the ESI;† the major matrix is confirmed to be $YbZn_{11}$.

Combining XRD and SEM results, micron-sized oxides with extremely small volume fraction primarily appear in cavities. Considering the extended grain size of the $YbZn_{11}$ crystals

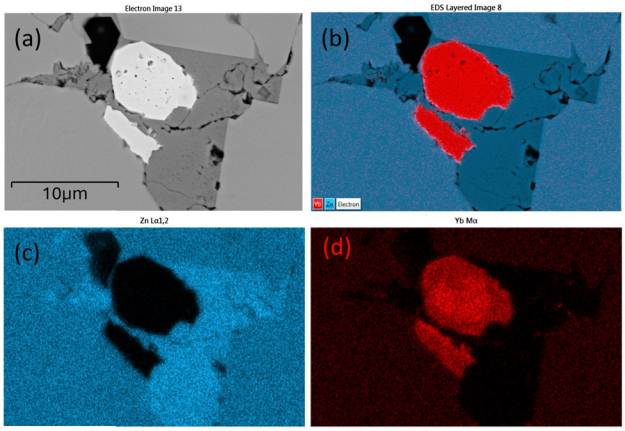

Fig. 3 EDS mapping. (a) BSE image of a typical defect site with cavities (black), Yb oxides (white), Zn (dark grey), and compared to $YbZn_{11}$ (light grey). (b) layered EDS map, (c) Zn distribution EDS map, and (d) Yb distribution map. The blue and red dots in (c) and (d) represent the relative Zn and Yb concentration.

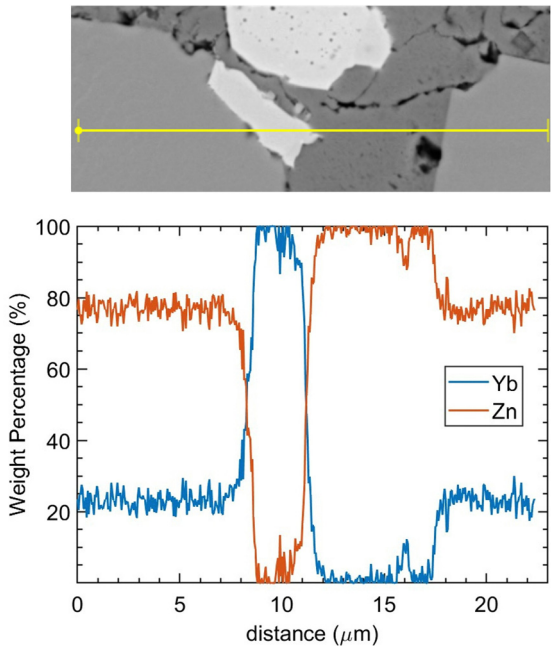

Fig. 4 EDS line scan on the defect site. The scanning line goes through the $YbZn_{11}$ matrix, Yb oxides (white), Zn-rich phase (dark grey), and $YbZn_{11}$.

(Fig. S1, ESI†), we believe that the scattered oxide impurities should not significantly affect the overall transport properties or the overall thermoelectric performance of macroscopic samples.

3.2 Band structure calculations

The electronic band structure and electronic density of states (DOS) calculated for intrinsic $YbZn_{11}$ are shown in Fig. 5. The band structure is shown in Fig. 5(a) along high symmetry direction $P(0.25,0.25,0.25)$–$N(0,0.50,0)$–$\Gamma(0,0,0)$–$M1/M(-0.50,0.50,0.50)$–Γ–$X(0,0,0.50)$–$P/M(0.50,0.50,0.50)$–$X1(0,1.00,0.50)$. The obtained DFT band structure and the DOS are in good agreement with previous calculations shown in the topological materials database.[23] The density of states has a smeared delta-function (Gaussian) shape centred approximately 322 meV below the Fermi level. This is an ideal band structure shape for a thermoelectric material as was discussed by Mahan and Sofo.[29] However, the Fermi level ideally should be within a few k_BT from the peak point where the slope of the DOS with respect to energy is maximum.

The Seebeck coefficient at room temperature (300 Kelvin) and the DOS are shown together in Fig. 5(b). The Mott formula

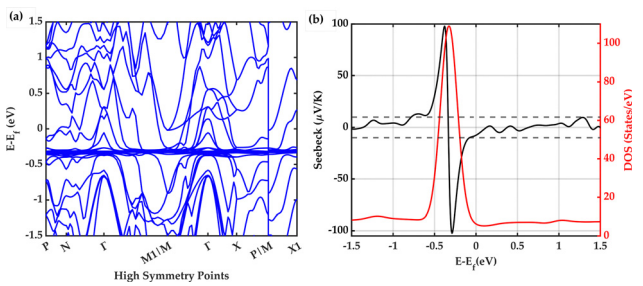

Fig. 5 (a) Electronic band structure and (b) Seebeck and density of states of $YbZn_{11}$.

for the thermoelectric power S for metals is defined in the following equation:

$$S_{\alpha\beta} = \frac{\pi^2}{3}\left(\frac{k_B^2 T}{e}\right)\left(\frac{\mathrm{d}\ln\sigma_{\alpha\beta}(\varepsilon)}{\mathrm{d}\varepsilon}\right)_{\varepsilon=\mu} \quad (2)$$

where k_B is the Boltzmann constant and the rest of the parameters are defined in eqn (1). Under constant relaxation time approximation, the Seebeck coefficient is directly proportional to the slope of the natural log of DOS. To achieve a high Seebeck coefficient, a large slope in the DOS near the chemical potential is required. Therefore, a delta function in a metallic material can potentially correspond to both high conductivity (due to high DOS) and a high Seebeck coefficient (due to large slope of DOS) values. Here we note that the Seebeck coefficient is in the range of -100 to 100 μV K^{-1} in a narrow chemical potential range ($\sim$500 meV). The main problem in this sample is that the intrinsic Fermi level is not close enough to the peak of the DOS. As shown in Fig. 5b, at the intrinsic level, the Seebeck coefficient is only -10 μV K^{-1}. Hence, the experimental intrinsic Seebeck coefficient is expected to be small. To reach higher Seebeck coefficient values, careful adjustment of the Fermi level *via* alloying and doping is needed.

For example, Fig. 6 demonstrates that upon doping with Al, we can shift the peak in the DOS to lower energies. Specifically, upon 4.5% Al doping, the peak is 371 meV below the Fermi level, which is 49 meV further away from the Fermi level compared to the intrinsic case. On the other hand, upon inclusion of zinc deficiency, we can move the peak toward the higher energies and closer to the Fermi level. Including 4.5% zinc vacancy shifts the peak to approximately -286 meV, bringing it closer to the Fermi level compared to the intrinsic case by 36 meV. In terms of the changes in the Seebeck coefficient, these two doping strategies should show opposite trends which we can confirm experimentally as will be discussed later. However, the predicted changes are not significant enough to increase the Seebeck coefficient significantly. To achieve a high Seebeck coefficient, the Fermi level must be shifted ideally to 202 meV below the intrinsic Fermi level where

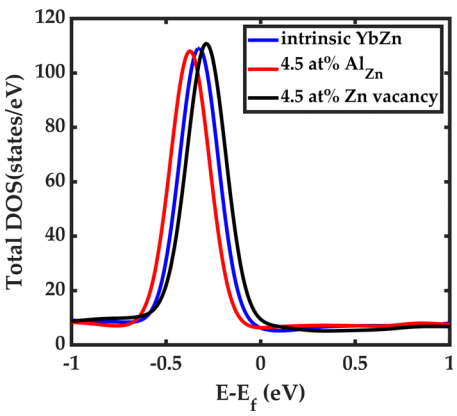

Fig. 6 Effect of Al doping and Zn deficiency on the density of states. Al doping shifts the DOS to lower energy levels while the Zn vacancy moves the DOS to higher energy levels.

the slope of the DOS is the largest. There may be other promising transition metals that could serve as dopants to fine-tune the Fermi level. Further research is necessary to optimally adjust the Fermi-level position, which will be the focus of future studies.

3.3 Performance

As discussed in the theoretical section, intrinsic YbZ_{11} is expected to have a low Seebeck coefficient. The room temperature value measured for intrinsic $YbZn_{11}$ is only 1 μV K^{-1}. Therefore, we attempted to tune the Fermi level *via* doping. We note that due to the errors in theoretical calculations for small Seebeck values and the presence of defects in experimental samples, a direct quantitative comparison of theory and experiment is not possible, and we can only use theory to predict trends.

In Fig. 7, the trend of measured room temperature Seebeck *versus* Al composition x ($YbZn_{11-x}Al_x$) is demonstrated. The addition of a small amount of Al improves the Seebeck of $YbZn_{11-x}Al_x$, peaking at $YbZn_{10.7}Al_{0.3}$. A further increase in the Al amount reduces the Seebeck coefficient. The low performance of samples with x higher than 0.3 could be attributed to the formation of other Yb–Al compounds due to limited solubility of Al in $YbZn_{11}$. However, due to their low concentration, they are not identified in the XRD analysis. The Seebeck value peaks at x = 0.3, reaching 9.54 μV K^{-1} at 300 K. After annealing, the Seebeck further increased by 24.4% to 11.87 μV K^{-1}, which should be attributed to improved distribution and dissolution of Al in Yb–Zn. Further high-temperature measurements after annealing are reported in the ESI,† Fig. S3, indicating further small improvements in the Seebeck coefficient.

Fig. 8 summarizes the trends of the transport properties, including the Seebeck coefficient, electrical resistivity, and thermal conductivity as a function of temperature from 50 to 400 K for Al-doped samples. The uncertainty on the Seebeck coefficient is less than 15% and for resistivity, it is less than 10%. These values are estimated by repeating the measurements under different thermal history conditions and are detailed in the ESI.† As temperatures increase, the Seebeck coefficient and resistivity both increase, a common trend in all samples studied here and in general in the thermoelectric field. The increasing Seebeck coefficient can be explained by the Mott

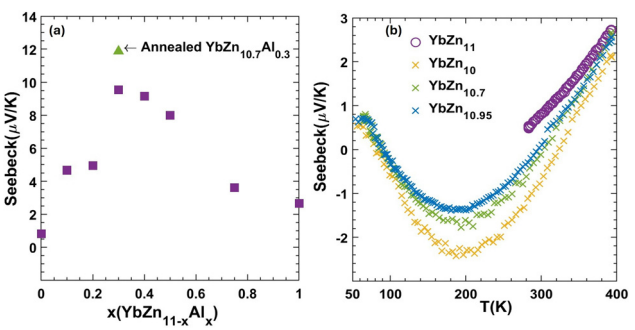

Fig. 7 (a) Room temperature Seebeck of $YbZn_{11-x}Al_x$ *versus* Al component x. The green triangle shows the annealed $YbZn_{10.7}Al_{0.3}$. (b) Seebeck of $YbZn_{11-x}$ (x = 0.05, 0.3, 1) *versus* temperature from 70–400 K.

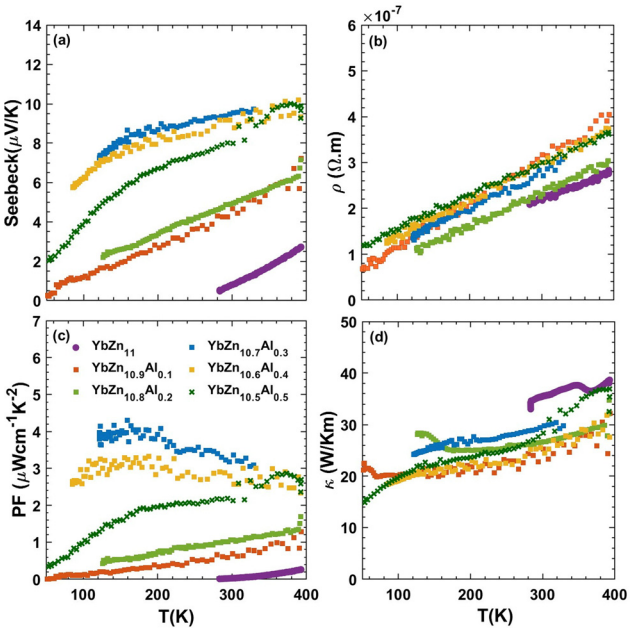

Fig. 8 (a) Seebeck coefficient, (b) resistivity, (c) power factor, and (d) thermal conductivity of $YbZn_{11-x}Al_x$ samples (x = 0, 0.1, 0.2, 0.3, 0.3, 0.4, 0.5) *versus* temperature from 70–400 K.

equation of metals (eqn (2)). Assuming no change in the slope of DOS with temperature, Seebeck should increase linearly with temperature. However, the relation is not exactly linear as the Fermi level position changes slightly with temperature. The increase in the resistivity can be explained by the increasing scattering between electrons and phonons at elevated temperatures. Finally, the thermal conductivity is dominated by the electronic contribution and follows the Wiedemann–Franz law closely. At room temperature, the electronic contribution of the thermal conductivity is 93% for the $YbZn_{11}$ sample and 88% for $YbZn_{10.7}Al_{0.3}$. Details of lattice thermal conductivity calculations and relevant plots are presented in the ESI.†

The addition of the optimal amount of Al (x = 0.3–0.5) altered the trend of the Seebeck coefficient *versus* temperature, particularly in the lower temperature range, resulting in a significant increase in the Seebeck coefficient. This increase is the primary reason for the enhanced power factor. The resistivities of all $YbZn_{11-x}Al_x$ samples closely resemble that of intrinsic $YbZn_{11}$, indicating only minor increases in scattering rates at low Al compositions. Further increasing the Al composition surpasses the solubility limit, and leads to different reactions during the melting process, resulting in the appearance of multiple crystalline oxides that increase the resistivity while the thermal conductivity remains close to intrinsic $YbZn_{11}$. More details are included in the ESI† (Fig. S8 and S9). The thermoelectric power factor of $YbZn_{11-x}Al_x$ (x = 0.3,0.4) peaks at around 100 K to 4 μW cm^{-1} K^{-2} due to the decreased resistivity at low temperatures and the sharp increase of the Seebeck coefficient.

Other ways of altering the $YbZn_{11}$ system such as non-stoichiometric composition $YbZn_{10.9}$ and Ag and Sn substitution $YbZn_{10.9}Sn_{0.1}$ have been tried. All show improvements but

do not exceed the $YbZn_{10.7}Al_{0.3}$ sample. Zn-deficient samples $YbZn_{11-x}$ with x = 0.05, 0.3, 1 were prepared using the same methods as those of intrinsic and Al-substitution samples. As shown in Fig. 7b, the introduction of Zn deficiency results in more negative Seebeck coefficient values. This is the opposite of what was observed with Al doping and is consistent with our theoretical results discussed in Section 3.2. Since Al-doping results in a shift of the DOS delta function to lower energy values and Zn-efficiency does the reverse (see Fig. 6), an opposite trend in the Seebeck coefficient is expected using these two doping strategies. While we can predict some trends using the first-principles approach, we acknowledge that a direct comparison between theory and experiment is not possible due to several factors. First, the as-grown $YbZn_{11}$ in the experiment is different from the ideal intrinsic $YbZn_{11}$ used in modelling, and the exact position of the Fermi level is unknown due to inherent low dimensional defects that are evenly distributed in the $YbZn_{11}$ crystal grains such as vacancies, substitutional impurities, and interstitials. As shown in the ESI,† changes in the inherent atomic-level defects/impurities results in changes in the DOS which alters the Seebeck coefficient at a given chemical potential. Second, first-principles data generated have an error bar due to errors in band structure calculations and the constant relaxation time approximation used. As seen in Fig. 8(a), the Seebeck coefficient does not show a linear trend with respect to temperature for many of the samples. This nonlinear trend can be attributed to temperature-dependent relaxation times as well as minor changes in the chemical potential with temperature and is discussed further in the ESI.† While we do not have a good way to estimate this error, the error in Seebeck calculations should be on the order of 10 $\mu V\ K^{-1}$ and therefore small Seebeck values as highlighted in the dashed-line region of Fig. 5(b) are close to the noise level of Seebeck calculations.

In the case of Zn deficiency, the value of the Seebeck coefficient is maximum at around 200 K, but its value remains small. The vacancies lowered both thermal and electrical conductivity slightly and, combined with low Seebeck values, did not result in improvements higher than that in the case of Al-doping. At x = 1 deficiency the hot-pressed sample shows a large level of cavities and poor sintering. Hence, Al-doping is identified as a better solution compared to the Zn-deficiency method. Similarly, Ag doping (not presented here) made the Seebeck coefficient more negative; however, Ag solubility is not good enough to significantly affect the Seebeck values toward high negative values.

Conclusions

$YbZn_{11}$-based samples were synthesized and confirmed using XRD and SEM methods. Small pores, Yb_2O_3, and zinc-rich defects were identified in the samples. The thermoelectric properties are reported for the first time. All samples have low resistivity confirming the metallic nature of the samples. The thermal conductivity of the samples is dominated by the electronic contribution as expected for metals with the intrinsic sample having a thermal conductivity of 35 $Wm\ K^{-1}$ at room temperature which further increasing with temperature. The downside of these samples is their low Seebeck coefficient values. Efforts to improve the Seebeck coefficient by Al substitution are conducted and resulted in improved Seebeck by an order of magnitude without sacrificing the electrical or thermal conductivity. However, the thermoelectric power factor remains modest with a peak value of 4 $\mu W\ cm^{-1}\ K^{-2}$ at 100 K. First-principles calculations identified a Gaussian-shape DOS ideal for the thermoelectric power factor in $YbZn_{11}$. However, the Fermi level is not ideally positioned with respect to this Gaussian function and needs to be adjusted for high performance. The limited solubility of Al, Sn, and Ag prevented further adjustments to the Fermi level. Similarly, zinc-deficiency tuning of the Fermi level is limited and does not allow for adjusting the Fermi level far enough to verify the existence of the DOS peak and, therefore, the high performance. Further studies of other dopants and alloying are needed to adjust the Fermi level to increase the Seebeck coefficient.

Author contributions

SL: conceptualization, data curation, formal analysis, investigation, methodology, visualization, writing – original manuscript. RQ and SSD: simulation, validation, writing – original manuscript. HW: data curation, formal analysis. JF: methodology, supervision, writing – review & editing, MZ: conceptualization, funding acquisition, project administration, supervision, and writing – review & editing.

Data availability

Data for this article, including raw experimental measurements, are available at $YbZn_{11}$ thermoelectric transport properties at **https://doi.org/10.18130/V3/QOPZXU**.

Conflicts of interest

There are no conflicts to declare.

Acknowledgements

RQ and SSD would like to acknowledge the Rivanna cluster of UVA used for the computational part. We acknowledge Xin Shi and Zhifeng Ren of the University of Houston for their help in verifying our results and for the high-temperature measurements presented in the ESI.† We acknowledge the Nanoscale Materials Characterization Facility (NMCF) at UVA for providing SEM and XRD facilities. This work is supported by NSF grant number 2230352.

Notes and references

1 Z. Zhang, X. Wang and Y. Yan, e-Prime - Advances in Electrical Engineering, *Electron. Energy*, 2021, **1**, 100009.

2 S. M. Sohel Murshed and C. A. Nieto de Castro, *Renewable Sustainable Energy Rev.*, 2017, **78**, 821–833.
3 ed H.-M. Tong, Y.-S. Lai and C. P. Wong.
4 M. J. Adams, M. Verosky, M. Zebarjadi and J. P. Heremans, *Phys. Rev. Appl.*, 2019, **11**, 054008.
5 M. Zebarjadi, *Appl. Phys. Lett.*, 2015, **106**, 203506.
6 H. J. van Daal, P. B. van Aken and K. H. J. Buschow, *Phys. Lett. A*, 1974, **49**, 246–248.
7 J. Mao, Y. Wang, H. S. Kim, Z. Liu, U. Saparamadu, F. Tian, K. Dahal, J. Sun, S. Chen, W. Liu and Z. Ren, *Nano Energy*, 2015, **17**, 279.
8 S. Li, K. Snyder, M. S. Akhanda, R. Martukanitz, M. Mitra, J. Poon and M. Zebarjadi, *Int. J. Heat Mass Transfer*, 2022, **195**, 123181.
9 F. Garmroudi, M. Parzer, A. Riss, C. Bourgès, S. Khmelevskyi, T. Mori, E. Bauer and A. Pustogow, *Sci. Adv.*, 2023, **9**(37), DOI: **10.1126/sciadv.adj1611**.
10 N. F. Mott, E. A. Davis and K. Weiser, *Phys. Today*, 1972, **25**, 55.
11 G. D. Mahan and J. O. Sofo, *Proc. Natl. Acad. Sci. U. S. A.*, 1996, **93**, 7436–7439.
12 J. Zhou, R. Yang, G. Chen and M. S. Dresselhaus, *Phys. Rev. Lett.*, 2011, **107**, 226601.
13 C. Jeong, R. Kim and M. Lundstrom, *J. Appl. Phys.*, 2011, **111**, 113707.
14 G. D. Mahan, *Solid State Phys.*, 1997, **51**, 81–157.
15 D. M. Rowe, V. L. Kuznetsov, L. A. Kuznetsova and G. Min, *J. Phys. D: Appl. Phys.*, 2002, **35**, 315.
16 E. Laube, *Monatsh. Chem.*, 1966, **97**, 722–732.
17 Z. Zhu and A. D. Pelton, *J. Alloys Compd.*, 2015, **641**, 261–271.
18 F. Akbar, I. Čurlík, M. Reiffers and M. Giovannini, *J. Alloys Compd.*, 2024, **976**, 173195.
19 I. Sakamoto, S. Ohara, I. Oguro, E. Yamamoto, Y. Haga, Y. Onuki and S. Maruno, *J. Alloys Compd.*, 1998, **275–277**, 505–509.
20 B. Bradlyn, L. Elcoro, J. Cano, M. G. Vergniory, Z. Wang, C. Felser, M. I. Aroyo and B. A. Bernevig, *Nature*, 2017, **547**, 298–305.
21 M. G. Vergniory, L. Elcoro, C. Felser, N. Regnault, B. A. Bernevig and Z. Wang, *Nature*, 2019, **566**, 480–485.
22 M. G. Vergniory, B. J. Wieder, L. Elcoro, S. S. P. Parkin, C. Felser, B. A. Bernevig and N. Regnault, *Science*, 2022, **376**(6595), DOI: **10.1126/SCIENCE.ABG9094**.
23 Topological materials database, **https://www.topologicalquantumchemistry.com/#/**.
24 P. Giannozzi, S. Baroni, N. Bonini, M. Calandra, R. Car, C. Cavazzoni, D. Ceresoli, G. L. Chiarotti, M. Cococcioni, I. Dabo, A. Dal Corso, S. de Gironcoli, S. Fabris, G. Fratesi, R. Gebauer, U. Gerstmann, C. Gougoussis, A. Kokalj, M. Lazzeri, L. Martin-Samos, N. Marzari, F. Mauri, R. Mazzarello, S. Paolini, A. Pasquarello, L. Paulatto, C. Sbraccia, S. Scandolo, G. Sclauzero, A. P. Seitsonen, A. Smogunov, P. Umari and R. M. Wentzcovitch, *J. Phys.: Condens. Matter*, 2009, **21**, 395502.
25 J. P. Perdew, K. Burke and M. Ernzerhof, *Phys. Rev. Lett.*, 1996, **77**, 3865–3868.
26 M. Topsakal and R. M. Wentzcovitch, *Comput. Mater. Sci.*, 2014, **95**, 263–270.
27 G. K. H. Madsen and D. J. Singh, *Comput. Phys. Commun.*, 2006, **175**, 67–71.
28 Y. B. Kuzma, P. I. Kripyakevich and D. P. Frankevich, *Izv. Akad. Nauk SSSR, Neorg. Mater.*, 1965, **1**, 1547–1553.
29 G. D. Mahan and J. O. Sofo, *Proc. Natl. Acad. Sci. U. S. A.*, 1996, **93**, 7436–7439.